Verifying national inventory-based combustion emissions of CO_2 across the UK and mainland Europe using satellite observations of atmospheric CO and CO_2

Tia R. Scarpelli[1,a], Paul I. Palmer[1,2,*], Mark Lunt[1,b], Ingrid Super[3], and Arjan Droste[3,4]

[1]School of GeoSciences, University of Edinburgh, Edinburgh, UK
[2]National Centre for Earth Observation, University of Edinburgh, Edinburgh, UK
[3]Department of Air quality and Emissions Research, TNO, Utrecht, The Netherlands
[4]Department of Water Management, Delft University of Technology, Delft, The Netherlands
[a]Now at: Carbon Mapper, Pasadena, CA, USA
[b]Now at: Environmental Defense Fund, Perth, Australia

Correspondence to: Paul I. Palmer (pip@ed.ac.uk)

Abstract. Under the Paris Agreement, countries report their anthropogenic greenhouse gas emissions in national inventories, used to track progress towards mitigation goals, but they must be independently verified. Atmospheric observations of CO_2, interpreted using inverse methods, can potentially provide that verification. Conventional CO_2 inverse methods infer natural CO_2 fluxes by subtracting *a~priori* estimates of fuel combustion from the *a~posteriori* net CO_2 fluxes, assuming that *a~priori* knowledge for combustion emissions is better than for natural fluxes. We describe an inverse method that uses measurements of CO_2 and carbon monoxide (CO), a trace gas that is co-emitted with CO_2 during combustion, to report self-consistent combustion emissions and natural fluxes of CO_2. We use an ensemble Kalman filter and the GEOS-Chem atmospheric transport model to explore how satellite observations of CO and CO_2 collected by TROPOMI and OCO-2, respectively, can improve understanding of combustion emissions and natural CO_2 fluxes across the UK and mainland Europe, 2018-2021. We assess the value of using satellite observations of CO_2, with and without CO, above what is already available from the *in~situ* network. Using CO_2 satellite observations leads to small corrections to *a~priori* emissions that are inconsistent with *in~situ* observations, due partly to the insensitivity of the atmospheric CO_2 column to CO_2 emission changes. When we introduce satellite CO observations, we find better agreement with our *in~situ* inversion and a better model fit to atmospheric CO_2 observations. Our regional mean *a~posteriori* combustion CO_2 emission ranges 4.6—5.0 Gt a^{-1} (1.5—2.4% relative standard deviation), with all inversions reporting an overestimate for Germany's wintertime emissions. Our national *a~posteriori* CO_2 combustion emissions are highly dependent on the assumed relationship between CO_2 and CO uncertainties, as expected. Generally, we find better results when we use grid-scale based *a~priori* CO_2:CO uncertainty estimates rather than a fixed relationship between the two species.

1 Introduction

More than 40% of the cumulative net CO_2 emissions from 1850 to 2019 have occurred since 1990, resulting in a global mean surface temperature rise of 0.45°C (IPCC, 2022). If the 2019 emission rate continues to 2030, we will have exhausted the remaining carbon budget to keep global mean temperatures within 1.5°C and depleted a third of the remaining carbon budget for 2°C (IPCC, 2022). These estimates assume that the land biosphere and ocean will continue to respond to changes in climate as they do today. The most effective lever at our disposal to rapidly reduce atmospheric concentrations of CO_2 is a commensurately large, rapid, and targeted reduction in emissions, as recognized by the Paris Agreement. A clearer understanding of the national importance of individual CO_2 emitting sectors is needed to develop effective emission mitigation policies. Similarly, global to regional observing networks are needed to verify the effectiveness of these policies to reduce national emissions from individual sectors. Here, we focus on the potential of satellite observations to verify changes in combustion emissions of CO_2 across the UK and mainland Europe.

Under the Paris agreement, countries annually report estimates of their anthropogenic greenhouse gas emissions in national inventories, typically with a lag of more than 12 months, as an approach to establish and track progress towards emission mitigation goals. These inventory-based estimates use 'bottom-up' methods that typically rely on national activity data (e.g., power plant fuel consumption) and country-specific emission factors (e.g., CO_2 emissions per unit of fuel consumed); the corresponding emission uncertainties are related to the underlying datasets and methodologies. To set effective national emission mitigation targets and track progress, it is important to estimate CO_2 combustion emissions accurately in these inventories, including accurate estimates of their uncertainties.

Observations of atmospheric CO_2 provide an independent evaluation of reported bottom-up CO_2 flux estimates (e.g., Peylin et al., 2013). A 'top-down' approach uses these atmospheric measurements to infer the most likely *a posteriori* distribution of CO_2 fluxes that would explain the observations, accounting for uncertainties associated with the measurements of the method. An atmospheric transport model is used to relate the gridded *a priori* estimates of CO_2 fluxes to 4-D distributions of atmospheric CO_2 concentrations. An observation operator is then applied to this 4-D distribution, which describes how a particular instrument samples the atmosphere at a given time and place. The resulting model atmospheric CO_2 measurements are then confronted with the observations, and the *a priori* flux estimates are adjusted to minimize any model-observation differences, resulting in *a posteriori* flux estimates that are consistent with *a priori* and measurement information. Ground-based *in situ* observations from the pan European measurement network have been used extensively to estimate regional net CO_2 fluxes (e.g., Scholze et al., 2019, Ramonet et al., 2020; Rödenbeck et al., 2020; Thompson et al., 2020).

Separating the combustion and natural components of the net *a posteriori* CO_2 flux estimates is non-trivial, which has resulted in a range of approaches being developed by researchers (e.g., Konovalov et al, 2016, Boschetti et al., 2018; Yang et al., 2023,

2

Feng et al, 2024). The most common approach is to assume we have near-perfect knowledge of anthropogenic emissions, subtract these *a priori* emission estimates from the net *a posteriori* values, and then interpret the residual as fluxes from the natural biosphere to compare with inventory estimates (e.g., White et al., 2019; Deng et al., 2022). The spatial and temporal information on both emissions and uncertainties are often highly uncertain but also needed to interpret atmospheric measurements (Super et al., 2020, Oda et al 2023). There is also now a greater focus on estimating changes in anthropogenic emissions, as countries introduce policies to decarbonize their economies.

With this impetus in mind, there is an urgent need to develop and evaluate robust methods that separate the combustion and natural influences on changes in atmospheric CO_2 at city-scale (e.g., Silva et al., 2013; Reuter et al., 2019; Goldberg et al., 2019; Yang et al., 2023) and national-scale (Palmer et al., 2006) using additional observations of trace gases co-emitted during the combustion process, e.g., CO and NO_2. Previous work has focused on using ground-based or aircraft *in situ* measurements of CO_2 and co-emitted trace gases (see references above), but we need to understand how we best use satellite observations to estimate anthropogenic emissions of CO_2, particularly in the context of the billion-euro investment in the Copernicus CO_2 Monitoring Mission, CO2M (Sierk et al., 2021).

Observations of atmospheric CO_2 collected by satellites have the advantage of global spatial coverage, subject to cloud cover, and have been used to constrain CO_2 flux estimates on the spatial scale of 1000s km (e.g., Chevallier et al., 2014; Feng et al., 2017; Chevallier et al., 2019; Palmer et al., 2019, Byrne et al, 2023). To date, few studies have focused on using these data to constrain CO_2 flux estimates over mainland Europe or the UK because there is less information about surface CO_2 on those spatial scales from the current generation of CO_2 satellites (OCO-2 and GOSAT) than the *in situ* measurement networks. This is in part because satellite observations of the atmospheric column of CO_2 are less sensitive to CO_2 surface fluxes compared to *in situ* measurement networks. It is widely anticipated that the significant increase in the volume and spatial coverage of data collected by CO2M will dramatically increase the competitiveness of satellite observations for estimating national-scale emissions across mainland Europe and the UK. CO2M will focus on quantifying anthropogenic emissions of CO_2 and methane and will form part of the European measurement and verification support capacity (Janssens-Maenhout et al, 2020). It will likely consist of three satellites, each with a push-broom imaging spectrometer that has an across-track swath of ~250 km with a spatial resolution of 4 km^2 (Sierk et al., 2021).

In this study, we quantify the ability of current satellite observations of CO_2 and CO to constrain country-scale combustion and non-combustion CO_2 flux estimates across the UK and mainland Europe. We use atmospheric CO_2 observations from the NASA OCO-2 instrument and CO observations from the ESA TROPOspheric Monitoring Instrument (TROPOMI) to estimate monthly CO_2 fluxes for 2018-2021. Our work is part of a larger effort to develop rigorous methods to evaluate nationally reported CO_2 emissions using *in situ* and satellite observations. In the next section, we describe the methods we use to infer

simultaneously combustion and natural fluxes of CO_2 using OCO-2 and TROPOMI data. Section 3 describes our results. We

100   conclude the paper in Section 4.

2 Data and Methods

Here, we describe the measurements we use to infer CO_2 fluxes across the UK and mainland Europe; the GEOS-Chem atmospheric chemistry transport model that describes the relationship between *a priori* inventories, atmospheric chemistry and transport, and the observed atmospheric concentrations of CO_2; and the ensemble Kalman Filter that is used to infer CO_2 fluxes

105   from *a priori* knowledge and the measurements. We describe the results from three inversions. For the first inversion we independently estimate *a posteriori* emissions of CO and CO_2. For the second and third inversions we assume combustion CO and CO_2 emission errors are correlated and report jointly estimated *a posteriori* CO and CO_2 fluxes. For the second inversion we assume a perfect correlation between these emissions errors and for the third inversion we use emission error correlations that are determined from sector-based errors in the bottom-up emission inventory (Super et al, 2024).

110

2.1 Satellite and *In Situ* Observations

For CO_2, we use observations of the atmospheric CO_2 column-averaged dry-air mole fraction (XCO_2) from the OCO-2 satellite, launched in 2014 (Crisp et al., 2017; Eldering et al., 2017). We use OCO-2 ACOS v10r data for 2018-2021 (OCO-2 Science

115   Team et al., 2020; Taylor et al., 2023). For CO, we use XCO observations from TROPOMI, July 2018 – December 2021, aboard the Sentinel-5P satellite, launched in 2017 (Veefkind et al., 2012; for CO retrieval: Vidot et al., 2012; Landgraf et al., 2016). For both satellite products, we filter observations as recommended in the Product User Guide, including a strict quality assurance flag value of >0.75 for TROPOMI XCO. We remove glint observations and those over the oceans and collate satellite columns and averaging kernels to a 0.25° x 0.3125° spatial grid to match model output (Figure 1). To compare our model

120   output to the satellite observations, we first sampled the model at the overpass time and location of each instrument. We then interpolate our model pressure levels to the satellite pressure levels and apply the scene-dependent retrieval averaging kernel to our 3-D model concentration fields. Different instrument sensitivities to CO and CO_2, described by their averaging kernels, are taken into account in the inversion framework described below.

125   We use *in situ* observations for 2018-2021 (Figure 1). We use the DECC surface measurement network in the UK (Stanley et al., 2018; Arnold et al, 2019; O'Doherty et al, 2019a,b) and the ICOS measurement network for Europe (ICOS R., 2022). We retain *in situ* observations collected between 0900 and 1800 local time – to avoid instances when tall tower inlets sit above a shallow boundary layer – and then time-average to 3-hourly intervals to match our GEOS FP model meteorology. All *in situ* sites have CO_2 observations, but some sites are missing CO observations. We additionally remove observations when the

130   atmosphere is not well-mixed. We consider the atmosphere to be well-mixed when the standard deviation of CO_2

4

concentrations across the lowest five vertical model levels is smaller than 0.3 ppm; this subjective value is based on three times the measurement precision of *in situ* measurements.

Figure 1 also shows European sites from the Total Carbon Column Observing Network (TCCON). Five sites are within our domain, including Bremen (Germany; Notholt et al, 2022), Karlsruhe (Germany; Hase et al, 2023), Nicosia (Cyprus; Petri et al, 2022), Orléans (France; Warneke et al, 2022), and Paris (France; Té et al, 2022). We use the TCCON observations as an independent comparison for our inversion results.

2.2 Forward Model Description

The forward model $\mathbf{H}$ describes the relationship between *a priori* flux estimates of CO_2 and CO and the atmospheric observations. We use the GEOS-Chem atmospheric chemistry transport model to relate surface fluxes of CO_2 and CO to 4-D atmospheric concentrations. We then sample these concentration fields at the time and location of measurements. In the case of satellite observations, we also use the scene-dependent averaging kernel to describe the instrument vertical sensitivity to changes in CO_2 and CO. Resulting sampled model atmospheric values can then be compared with observations:

$$\mathbf{y} = \mathbf{H} \cdot \mathbf{x} \quad (1)$$

where $\mathbf{y}$ denotes the observation vector, and $\mathbf{x}$ denotes the state vector that includes our *a priori* CO_2 and CO flux estimates.

We use the GEOS-Chem version 12.5.2 atmospheric chemistry and transport model which we run at 0.25° x 0.3125° resolution for a nested European domain (-15 to 35° E longitude and 34 to 66° N latitude) with 47 vertical levels. GEOS-Chem is driven by GEOS FP meteorological re-analyses fields from the NASA Global Modelling and Assimilation Office (GMAO) Global Circulation Model.

Our *a priori* flux estimates ($\mathbf{x}$) include all sources contributing to observed atmospheric CO_2 and CO. Equation 2 shows the sources for CO_2 including combustion emissions ($CO_2^{Combust}$), non-combustion fluxes (both biogenic and non-combustion anthropogenic sources; CO_2^{Bio}), and background CO_2 that is transported to and from our domain (CO_2^{Trans}). Atmospheric CO sources include combustion emissions ($CO^{Combust}$), transport (CO^{Trans}), and production of CO through oxidation (CO^{Chem}), as shown in equation 3.

$$CO_2 = CO_2^{Trans} + CO_2^{Combust} + CO_2^{Bio} \quad (2)$$
$$CO = CO^{Trans} + CO^{Combust} + CO^{Chem} \quad (3)$$

For our 2018-2021 *a priori* fluxes, we use a combination of regional and global inventories (Figure 2). Combustion emissions for both species ($CO_2^{Combust}$ and $CO^{Combust}$) are from the TNO (Nederlandse Organisatie voor Toegepast Natuurwetenschappelijk Onderzoek; Netherlands Organisation for Applied Scientific Research) GHGco v5.0 emission inventory at 0.1° x 0.05° resolution (Super et al., 2020; Kuenen et al., 2022) with national totals based on emissions reported in national inventories and extrapolated from 2019 to more recent years; 2019 represents the latest year for which we have air pollution and greenhouse gas inventories (Kuenen et al, 2022). We apply scaling factors provided by TNO to reflect monthly, hourly, and daily patterns in emissions by sector with the same scaling factors used for each year. Our combustion source also includes biomass burning emissions from the GFAS v1.2 inventory (Kaiser et al., 2021). Non-combustion fluxes (CO_2^{Bio}) include ocean fluxes from the NEMO-PISCES model (Lefèvre et al., 2020), lateral carbon fluxes related to crop removal (Deng et al., 2022), and hourly terrestrial biosphere fluxes at 1/120° x 1/60° resolution produced by the VPRM model following methods described by Gerbig (2021) driven by ERA5 meteorology. We include non-combustion (e.g., fugitives) anthropogenic emissions from the TNO inventory in our non-combustion fluxes. Fugitive emissions of CO_2 are typically very small, e.g., escape from agricultural greenhouses enriched with CO_2.

For our nested domain, we use lateral boundary conditions for CO_2 (CO_2^{Trans}) from the CAMS inversion-optimized global greenhouse gas analysis with assimilation of *in situ* observations (Chevallier, 2020). Our boundary conditions for CO (CO^{Trans}) are from the CAMS global reanalysis (Inness et al., 2019). We use the CAMS fields at their provided temporal resolution (3-hourly) and re-grid them to the GEOS-Chem horizontal spatial resolution of 2° x 2.5° so we can use them as boundary conditions for our finer-resolution nested model, centred over Europe. Because the vertical resolution of GEOS-Chem does not align with CAMS, we translate the CAMS native vertical resolution to our 47 model layers using linear interpolation of logarithmic pressure values. We fill in the species concentrations at the lowest or highest pressure level in CAMS for the top or surface of the atmosphere, respectively, when the GEOS-Chem pressure levels go beyond the bounds of CAMS.

We treat the relationship between surface fluxes and concentrations (equation 1) as linear (e.g., a doubling of emissions leads to a doubling of the atmospheric signal). To linearize the CO simulation, we use offline chemistry terms to represent the chemical production of CO (CO^{Chem}). CO is primarily produced by oxidation of methane and non-methane volatile organic compounds by the hydroxyl radical (OH), so we generate the production terms using offline 3-D loss fields of OH generated from a previous GEOS-Chem full-chemistry simulation (Fisher et al., 2017).

2.3 Inverse Model Description

For our inversion, we use the Ensemble Kalman Filter (EnKF) approach as discussed in detail by others (e.g., Peters et al., 2005; Hunt et al., 2007; Feng et al., 2009; Liu et al., 2016). We specifically follow the methods derived by Hunt et al. (2007) and summarized by Liu et al. (2016) for the Local Ensemble Transform Kalman Filter (LETKF).

205   We solve the inversion in ensemble space rather than for the state vector elements. For each state vector element, we have an ensemble of potential scale factors that follow our prescribed error statistics. For each assimilation time-period (over which we ingest observations), we solve for the mean *a posteriori* state vector ($\mathbf{x}^a$) that represents the mean of our N ensemble members (where we use $N = 100$):

210     $$\mathbf{x}^a = \mathbf{x}^b + \mathbf{K}(\mathbf{y}_{obs} - \mathbf{y}^b), \quad (4)$$

where $\mathbf{x}^a$ and $\mathbf{x}^b$ are the means across ensemble members for our *a posteriori* and *a priori* state vectors, respectively. We use error statistics, as described in Section 2.4, to generate the *a priori* state vector ensemble members. $\mathbf{y}_{obs}$ is the observation vector and each element of $\mathbf{y}^b$ is the mean of model-predicted concentrations across N ensemble members. For the nth

215   ensemble member ($\mathbf{x}_n^b$), the model-predicted concentrations are $\mathbf{y}_n^b = H(\mathbf{x}_n^b)$.

$\mathbf{K}$ describes our Kalman gain matrix that regulates the degree to which any disagreement between model and observation will adjust the state vector. We determine $\mathbf{K}$ using the matrix $\mathbf{X}^b$, which describes the difference between the ensemble members and their mean, and the matrix $\mathbf{Y}^b$, which describes the difference between the model-predicted concentrations and their mean:

220

$$\mathbf{K} = \mathbf{X}^b \mathbf{P}^a (\mathbf{Y}^b)^T \mathbf{R}^{-1}, \quad (5)$$

where the nth column of $\mathbf{X}^b$ is $\mathbf{x}_n^b - \mathbf{x}^b$ and the nth column of $\mathbf{Y}^b$ is $\mathbf{y}_n^b - \mathbf{y}^b$ (each column representing an ensemble member). $\mathbf{R}$ is the observation error covariance matrix, which includes the errors from our forward model, estimates based on

225   prior studies, and from observations. For CO_2, we use an *a priori* model error of 1.5 ppm for the satellite inversion (Feng et al., 2017) and 3 ppm for the *in situ* inversion (within the range of Monteil et al., 2020 and White et al., 2019). For CO, we use an *a priori* model error of 15 and 20 ppb for the satellite and *in situ* inversions, respectively (Northern Hemisphere CO column and surface mole fraction model-observation differences from Bukosa et al., 2023). For the observations, we use the errors as provided for the satellite or *in situ* network, averaged to the model resolution. We generate the off-diagonal covariance for $\mathbf{R}$

230   based on the spatial and temporal proximity of observations following an exponential decay with spatial and temporal length scales of 100 km and 4 hours, respectively; these values are based on our preparatory work (not shown) using this model definition.

The $\mathbf{P}^a$ matrix is a representation of the *a posteriori* error covariance in ensemble space:

235

$$\mathbf{P}^a = [(N - 1)\mathbf{I} + (\mathbf{Y}^b)^T \mathbf{R}^{-1} \mathbf{Y}^b]^{-1}, \quad (6)$$

7

Deleted: .

where $\mathbf{I}$ is an identity matrix and N is our number of ensemble members. $\mathbf{P}^a$ is used to determine the *a posteriori* ensemble members ($\mathbf{X}^a$) where the nth column of $\mathbf{X}^a$ is $\mathbf{x}_n{}^a - \mathbf{x}^a$ and the error covariance matrix ($\mathbf{P}^a$):

$$\mathbf{X}^a = \mathbf{X}^b[(N-1)\mathbf{P}^a]^{1/2} \quad (7)$$
$$\mathbf{P}^a = \mathbf{X}^a(\mathbf{X}^a)^T(N-1)^{-1}. \quad (8)$$

We use an assimilation window of two weeks and a lag window of one month, accounting for the impact of historical emissions on our assimilation period. This means that the state vector for each time-step includes scale factors for the assimilation window and lag window. Our preparatory work revealed that using a lag window longer than a month did not significantly impact our results because signals by that time have decayed substantially (not shown). We perform our inversion sequentially, using the *a posteriori* scale factors for a given assimilation window to update the *a priori* scale factors for the next lag window over the same date range. To avoid unrealistically small prior uncertainties, we apply a 10% error inflation when we update the *a priori* state vector.

The benefit of the LETKF is that we can localize the inversion so that each state vector element is only influenced by a subset of observations. For our inversions using *in situ* observations, we localize by distance so that each state vector element that represents a grid-scale variable is only influenced by observations within a 1000 km range. We chose that upper limit as a compromise to ensure we included observations that had the most sensitivity to the emissions and to discard observations with much smaller sensitivities that potentially could introduce spurious correlations.

2.4 Description of Inverse Model Experiments

We test different approaches to investigate the usefulness of satellite observations for evaluating CO_2 combustion emissions. The approaches vary in the observations that are used and the representation of error covariances for our *a priori* estimates. For each type of inversion, we compare our satellite inversion results to comparable inversions using *in situ* observations.

In the inversions, instead of solving for CO_2 or CO fluxes, we solve for scale factors that scale up or scale down the source terms from equations 2-3. We first assume that our *a priori* scale factors are all equal to one. We solve for *a posteriori* scale factors that, when applied to our source terms, will result in modelled atmospheric CO_2 or CO concentrations in better agreement with observations.

For our first approach (CO_2-only), we perform a CO_2-only inversion that assimilates CO_2 observations. Our state vector includes scale factors for the sources of equation 2:

8

$$\mathbf{x}_{co2} = \left(\mathbf{x}_{co2}{}^{Trans}, \mathbf{x}_{co2}{}^{Bio}, \mathbf{x}_{co2}{}^{Combust}\right) \quad (9)$$

275   where $\mathbf{x}_{co2}{}^{Bio}$ and $\mathbf{x}_{co2}{}^{Combust}$ are a vector of scalers, common to all inversions, with each element applying to a non-combustion or combustion grid cell at 0.5° x 0.625° resolution (Appendix A). The four transport scale factors for CO_2 (and four for CO), described by $\mathbf{x}_{co2}{}^{Trans}$, common to all our inversion calculations, applies to the four lateral boundary conditions of the nested model domain.

280   In our second approach (Joint CO_2:CO), we perform a joint CO_2:CO inversion that assimilates both CO_2 and CO observations. For the joint inversion, we assume there is 100% correlation for the CO_2 and CO combustion emission errors. This means any adjustment made by our inversion to the CO_2 combustion scale factors will also apply to the CO scale factors and vice versa. We can then use a common combustion scaling term for both species in our state vector ($\mathbf{x}^{Combust}$). We do not account for the atmospheric CO_2 production from the oxidation of CO and other reduced carbon species (Suntharalingam et al, 2005). Our

285   state vector also includes four scale factors for lateral boundary transport of each species (as described above). For CO we also include two scale factors to the state vector for the chemistry terms ($\mathbf{x}_{co}{}^{Chem}$), describing the secondary production of CO from the oxidation of methane and non-methane volatile organic compounds. The two scale factors reflect differences in their emission distributions and atmospheric lifetimes. The CO_2 and CO state vectors are described as:

290     $$\mathbf{x}_{co2} = \left(\mathbf{x}_{co2}{}^{Trans}, \mathbf{x}_{co2}{}^{Bio}, \mathbf{x}^{Combust}\right) \quad (10)$$
$$\mathbf{x}_{co} = \left(\mathbf{x}_{co}{}^{Trans}, \mathbf{x}_{co}{}^{Chem}, \mathbf{x}^{Combust}\right). \quad (11)$$

For our first two approaches, we assume an *a priori* uncertainty of 20% (relative standard deviation) for the combustion scale factors ($\mathbf{x}^{Combust}$). We use an *a priori* uncertainty of 50% for the non-combustion scale factors ($\mathbf{x}_{co2}{}^{Bio}$), and 5% for the

295   atmospheric transport and chemistry scale factors. These are informed estimates based on our previous work, e.g., Feng et al, (2017). For our non-combustion and combustion scale factors, we generate error covariances for nearby grid cells that exponentially decays with increasing distance. Our method for generating the error covariance matrix based on these uncertainties is described in detail in Appendix A.

300   We acknowledge that the assumption of 100% error correlation for CO_2 and CO combustion emissions is likely to be a gross overestimate, but it serves as an illustrative upper limit for our calculations. For example, we may underestimate CO emissions due to an underestimate of incomplete combustion activities, and this will not translate to the same underestimate in CO_2.

For our third approach (TNO $CO_2:CO$), we test this assumption by solving for the CO_2 and CO combustion scaling terms separately:

320
$$\mathbf{x}_{co2} = \left(\mathbf{x}_{co2}{}^{Trans}, \mathbf{x}_{co2}{}^{Bio}, \mathbf{x}_{co2}{}^{Combust}\right) \ (12)$$
$$\mathbf{x}_{co} = \left(\mathbf{x}_{co}{}^{Trans}, \mathbf{x}_{co}{}^{Chem}, \mathbf{x}_{co}{}^{Combust}\right) \ (13)$$

We call this our TNO approach because we use estimates of the uncertainties in the TNO emission inventory to create our error covariance matrix (Super et al., 2024). We increase the provided uncertainties by a factor of three to make them more

325   comparable with our other simulations. This results in a mean grid-scale CO_2 combustion uncertainty of 18%, though there is greater variability in grid cell uncertainties compared to our other approaches. We expect higher correlation between CO_2 and CO gridded emissions in regions where the same spatial product, e.g., road network maps, is used to distribute emissions for both species and that spatial product has high uncertainties. The spatial products and how they are used to distribute air pollutant emissions is described by Kuenen et al (2022).

330

3 Results and Discussion

First, we describe the comparison between our *a priori* and *a posteriori* model simulations against observations. We then report our *a posteriori* CO_2 fluxes for Europe and its constituent countries and the UK.

335

3.1 Inversion performance

Our *a priori* CO_2 emissions are already consistent with data from the five relevant TCCON sites (locations shown in Figure 1; Pearson correlation coefficient R= 0.87), and *in situ* (R=0.76) and satellite (R=0.84) observations. The model has a small,

340   positive relative mean bias compared to TCCON (0.7%) and a very small bias compared to *in situ* and satellite observations (0.2%). Table A1 reports a statistical summary of the model-observation comparisons. The satellite inversions show improvement for the model-satellite fit (R=0.92-0.95), as expected, and the model-*in situ* fit (R=0.80-0.82). Similarly, the *in situ* inversions improve model-*in situ* fit (R=0.83-0.84) and to a lesser extent the model-satellite fit (R=0.85-0.87).

345   In general, including CO and TNO uncertainty estimates improves the model-observation fit and reduces the mean bias. For example, the satellite joint $CO_2:CO$ (R=0.93) and TNO (R=0.92) inversions show the greatest improvement in fit with TCCON. The one exception is that the mean bias compared to TCCON is slightly larger with CO (0.3-0.5%) compared to CO_2-only (0.2-0.4%), a small difference that is likely a result of introducing the $CO:CO_2$ error correlation. The TCCON CO_2 bias is seasonal (not shown) with the *a priori* model showing no bias in July-August and a positive bias of 1-4 ppm for the rest of the

350   year. The *in situ* inversions reduce the mean bias for March-June by 1 ppm, and this improvement lines up with a reduction in

the biosphere sink for these inversions (discussed later). We also compare our *a priori* and *a posteriori* fields with TROPOMI CO but the improvement is marginal. The Pearson correlation coefficient between the *a posteriori* model and *in situ* data increases by 4% for the joint CO_2:CO inversion and by 5% for the TNO joint inversion. For a similar comparison but using satellite data, the correlation coefficient increases by 6% for the joint CO_2:CO inversion and by 4% for the TNO joint inversion.

We also assess inversion performance by the degree of uncertainty reduction for the *a posteriori* CO_2 combustion emission estimates. Table 1 shows *a posteriori* uncertainties for our domain-scale CO_2 combustion emissions. The reductions in relative uncertainty achieved at the domain scale for all inversions are small (6-12%) with the CO_2-only and TNO satellite inversions showing no reduction. The TNO inversions show smaller reductions in uncertainty (0-6%) compared to the joint inversions (8-12%), but they also start with a lower *a priori* uncertainty at 1.6% (relative standard deviation; RSD = sample standard deviation/sample mean) compared to 2.4% for non-TNO *a priori* uncertainties.

At the national scale, we see the greatest uncertainty reduction in CO_2 combustion emissions for the top 10 emitting countries when satellite CO observations or *in situ* CO_2 measurements are included and the non-TNO uncertainties are used (Table A2 and A3). The average uncertainty reductions for the joint satellite and CO_2-only *in situ* inversions are 11% and 9%, respectively. This is not surprising given the greater number of observations provided by these two platforms and increased sensitivity to surface fluxes compared to OCO-2. Including *in situ* CO observations in the inversion does not improve the national-scale uncertainty reduction. Because we use lower *a priori* uncertainties in the TNO inversion (national-scale 2-10% RSD) compared to the other inversions (6-14% RSD), fewer countries have reduced uncertainties for the TNO inversion, though *a posteriori* uncertainties are reduced in the Netherlands (2%) for both in-situ and satellite compared to *a priori* uncertainties (3%).

3.2 Emission Estimates for the UK and mainland Europe

Table 1 shows our mean domain-scale (includes the UK and mainland Europe) combustion emissions for 2018-2021. The inversions show a small decrease or no change from the *a priori* emissions (4.9 Gt a^{-1}), except for the joint satellite and *in situ* inversions that show a larger decrease (4.6 Gt a^{-1}) and an increase (5.0 Gt a^{-1}) from the *a priori*, respectively. Figure 3 shows that the joint satellite inversion decreases combustion emissions year-round for all years with the greatest decreases in winter. The TNO satellite/*in situ* and CO_2-only *in situ* inversions also show decreases in the winter and early spring (Figures 3 and 4), providing more confidence in this scaling down of emissions.

In contrast, the joint *in situ* inversion is higher than the *a priori* values for all months and all years (Figure 4). This pattern is not reflected in our other inversion approaches and is likely, in part, due to the model underestimating the fine-scale variability in CO compared to what is measured at some *in situ* sites combined with the use of a common scale factor for both CO and

11

CO_2, leading to an over-correction upward of combustion emissions. For example, we find that removing a single site close to an urban region in northern Italy (Ispra ICOS site) reverses the sign of scaling in the region from an increase to a decrease. The disagreement between satellite and *in situ* CO_2:CO inversions is less pronounced for the TNO inversions because the separation of CO_2 and CO in our state vector prevents the CO underestimates from heavily influencing the CO_2 combustion emissions.

Figure 3 shows a slight (1%) decrease in mean *a priori* combustion emissions from 2018 to 2021, and all satellite and *in situ* inversion results show a similar trend (Figure 3 and 4). The mean *a priori* non-combustion (biogenic) CO_2 sink shows a slight increase (1%) for 2018-2021, and the inversion results show a similar (satellite; Figure 3) or greater increase (*in situ*; Figure 4*)* in the CO_2 sink. Figure 4 shows the monthly mean biogenic CO_2 sink is weakened for the *in situ* inversions, mostly in summer, whereas Figure 3 shows almost no change in the sink for the satellite inversions (also listed in Table A4), indicating that the CO_2 *in situ* observations, due to the coverage and sensitivity they provide, are needed for constraining biogenic flux estimates.

The differences between *a posteriori* and *a priori* annual emissions for all inversions except the joint satellite inversion are not statistically significant and remain within the 1-σ uncertainties of the *a priori* estimate. The inter-annual trends are also smaller in magnitude than the *a posteriori* uncertainties, making it difficult to assess if CO_2 combustions in Europe have decreased from 2018 to 2021. For the joint satellite and *in situ* inversions, we assumed that CO was a strong tracer for CO_2 combustion emissions on this regional scale by using a common scale factor, but we find that this assumption leads to more extreme, likely unrealistic, divergence from the *a priori*, in disagreement with the other inversion results. This reflects the difficulties of using CO as a tracer for CO_2 combustion emissions at regional scales, and the importance of error characterization.

3.3 National-scale Emission Estimates

Figure 5 shows national CO_2 combustion emissions for the top 10 emitting countries in our European domain (also listed in Tables A2 and A3). Germany is the highest emitter with an *a priori* emission of 821 Tg a^{-1}. Most inversions show a decrease in Germany's emissions (717-806 Tg a^{-1}) except for the *in situ* joint inversion which shows an increase (830 Tg a^{-1}) and the CO_2-only inversion which shows little change from the *a priori* estimate (819 Tg a^{-1}). The other top emitting countries, including Poland, the UK, France, Italy, Spain, Belgium, the Czech Republic, the Netherlands, and Romania, show emission decreases for the satellite joint (3-17%) and TNO (0-4%) inversions. The *in situ* CO_2-only and TNO inversions generally show only small changes (<1%) in national emissions except for a 4% national emission decrease in the Netherlands and Belgium for the CO_2-only inversion.

12

The joint inversions show the largest changes in national emissions but in opposite directions. In contrast, the TNO inversions show smaller changes from the *a priori* (in part, due to the lower *a priori* uncertainties) and better agreement, including agreement in Germany where there is greater divergence from the *a priori* estimate (2% decrease for both TNO inversions).

Despite the national-scale disagreements for some inversions, we find regional corrections to combustion emissions are consistent for all inversions. Figure 6 shows that the populated North Rhine-Westphalia region in western Germany shows *a posteriori* CO_2 combustion emission estimates are smaller than *a priori* values for all inversions. The TNO and CO_2-only inversions show mixed corrections in Poland with TNO inversions showing the best agreement. Most inversions, including both TNO inversions, show an increase in emissions near Milan and Vienna, but over other major cities like Paris, Madrid, and London there is less agreement in the sign and magnitude of the emissions changes.

The differences in the joint inversions are due to contrasting corrections to CO emissions that carry over into the CO_2 emissions. Figures A1 and A2 show that the *in situ* joint inversion shows decreases for high-emitting regions in Europe for winter and spring, but this is mostly offset by large emission increases in summer and fall. In contrast, the satellite joint inversion shows decreases for all seasons. For the TNO inversion, there is less disagreement between the seasonal emissions corrections for CO_2, but there are disagreements in CO corrections. Figure A3 shows the CO corrections for the TNO inversion generally occur at the national-scale and we know there is low error correlation between the two species at the national-scale (Super et al., 2024), so it is not surprising that these corrections do not carry over to CO_2. The improvement in the agreement between our *a posteriori* CO emissions and TROPOMI and *in situ* CO measurements, relative to our *a priori* emissions, is larger than for the similar comparison using CO_2. This reflects the larger assumed CO errors. *A posteriori* CO estimates agreed better with these measurements for the joint CO_2:CO and the TNO inversions, with the TNO inversion performing slightly better.

Figure 7 shows national non-combustion (biogenic) emissions for the countries in Figure 5. All countries show a net sink with France having the largest net sink. The *in situ* inversions tend to decrease (lessen) the CO_2 sink for all countries and reduce uncertainties. Figure 8 shows the spatial pattern in the flux changes is consistent for all *in situ* inversions. In contrast, the national CO_2 biogenic fluxes show little change from the *a priori* for the satellite inversions, highlighting the importance of *in situ* CO_2 observations for constraining biogenic flux estimates. For all inversions, the CO_2 sink in northern Germany is strengthened (more negative fluxes) and weakened in southern Germany and Switzerland, though there are conflicting corrections in surrounding regions such as France and northern Italy. These disagreements may be due to the differing observing capacities with satellites having seasonal limitations due to snow and clouds. We find low *a posteriori* error correlations between national-scale combustion and biogenic fluxes (mostly R<0.1, except for Germany R=-0.2), indicating that the disagreement in *in situ* and satellite *a posteriori* biogenic fluxes will not carry over into combustion emission estimates.

4 Conclusions

460 We find that using CO_2 satellite observations from OCO-2 alone cannot reproduce *a posteriori* European CO_2 fluxes inferred from the European *in situ* CO_2 measurement network. The satellite observations (CO_2-only) do not show significant combustion emissions changes from our *a priori* estimates, whereas when we use *in situ* CO_2 or CO_2 and CO satellite observations, we see greater divergence from the *a priori* emissions. This is likely due to *in situ* data being more sensitive to emissions and to coverage provided by the current generation of satellites being insufficient to update significantly the state

465 vector. We find that the *in situ* network is still essential for constraining biogenic fluxes, though we also find low correlation between combustion and biogenic fluxes indicating that our inability to constrain the biogenic flux estimate using satellites does not prevent the estimation of combustion emissions at the national scale using satellite observations.

All our inversions indicate that CO_2 combustion emissions for regions of Germany are overestimated in winter, and most

470 inversions show this overestimate extends to other countries in Europe. We also find that the *in situ* inversions show a smaller summertime European CO_2 sink which is not shown for the satellite inversions. We find that the existing observational networks are not able to significantly reduce the errors for our European or national emission estimates to the extent necessary for distinguishing inter-annual emission trends that represent only a few percent of total emissions.

475 When using CO as a tracer for CO_2 combustion emissions in our inversion system, we find that our interpretation of inversion results is highly dependent on the assumptions of *a priori* error correlation between CO and CO_2. The use of a $CO:CO_2$ inversion system can potentially improve our ability to track CO_2 combustion emissions provided we have well-characterized error correlations between the two species which may require broad measurement based studies to determine the error correlations specific to a source and region. This suggests that the increase in observational capacity for CO_2 and co-emitted

480 trace gases promised by the Copernicus CO_2 Monitoring (CO2M) satellite mission has the potential to improve our ability to constrain national combustion emission estimates provided that the error correlations for CO_2 combustion emissions and the co-emitted species are strong and well characterized using empirical data.

In general, the improvements in model-observation fit are small and we do not see significant reduction in uncertainties

485 compared to our *a priori* estimates. This is expected because we have extensive knowledge about sector emissions that underpin these regional inventories, reflected in the small uncertainties associated with combustion emission estimates across the UK and mainland Europe. The use of CO observations and TNO error estimates leads to better agreement between satellite and *in situ* inversions and the best model-observation fit, though including CO does not reduce the model bias compared to TCCON and likely reflects the need for *in situ* CO_2 observations for reducing biases related to biogenic fluxes. Despite the

490 sensitivity of our *a posteriori* emission estimates to the choice of *a priori* CO_2 and CO uncertainties, the joint and TNO satellite inversions perform similarly when compared to TCCON. This highlights the need for not only further satellite observing

14

capacity but also improved ground-based networks for evaluating satellites and the usefulness of including co-emitted species observations.

505

References

Arnold, T.; Rennick, C.; O'Doherty, S.; Say, D.; Young, D.; Stavert, A.; Wenger, A. (2019): Deriving Emissions related to Climate Change Network: CO_2, CH_4, N_2O, SF_6 and CO measurements from Heathfield Tall Tower, East Sussex. Centre for Environmental Data Analysis.

510 Balsamo, G., Engelen, R., Thiemert, D., Agusti-Panareda, A., Bousserez, N., Broquet, G., Brunner, D., Buchwitz, M., Chevallier, F., Choulga, M., Denier Van Der Gon, H., Florentie, L., Haussaire, J.-M., Janssens-Maenhout, G., Jones, M. W., Kaminski, T., Krol, M., Le Quéré, C., Marshall, J., McNorton, J., Prunet, P., Reuter, M., Peters, W., and Scholze, M.: The CO2 Human Emissions (CHE) Project: First Steps Towards a European Operational Capacity to Monitor Anthropogenic CO2 Emissions, Frontiers in Remote Sensing, 2, 707247, https://doi.org/10.3389/frsen.2021.707247, 2021.

515 Boschetti, F., Thouret, V., Maenhout, G. J., Totsche, K. U., Marshall, J., and Gerbig, C.: Multi-species inversion and IAGOS airborne data for a better constraint of continental-scale fluxes, Atmos. Chem. Phys., 18, 9225–9241, https://doi.org/10.5194/acp-18-9225-2018, 2018.

Bukosa, B., Fisher, J. A., Deutscher, N. M., and Jones, D. B. A.: A Coupled CH4, CO and CO2 Simulation for Improved Chemical Source Modeling, Atmosphere, 14(5), 764, https://doi.org/10.3390/atmos14050764, 2023.

520 Byrne, B., et al: National CO2 budgets (2015–2020) inferred from atmospheric CO2 observations in support of the global stocktake, Earth Syst. Sci. Data, 15, 963–1004, https://doi.org/10.5194/essd-15-963-2023, 2023.

Chevallier, F.: Description of the CO2 inversion production chain 2020, Copernicus Atmosphere Monitoring Service (CAMS), Accessed: January 2023, available at https://atmosphere.copernicus.eu/greenhouse-gases-supplementary-products, 2020.

Chevallier, F., Remaud, M., O'Dell, C.W., Baker, D., Peylin, P., and Cozic, A.: Objective evaluation of surface- and satellite-525 driven carbon dioxide atmospheric inversions, Atmos. Chem. Phys., 19, 14233–14251, https://doi.org/10.5194/acp-19-14233-2019, 2019.

Chevallier, F., Palmer, P.I., Feng, L. Boesch, H. O'Dell, C., and Bousquet, P.: Towards robust and consistent regional CO2 flux estimates from in situ and space-borne measurements of atmospheric CO2, Geophys. Res. Lett., 41, https://doi.org/10.1002/2013GL058772, 2014.

530 Crisp, D., Pollock, H. R., Rosenberg, R., Chapsky, L., Lee, R. A., Oyafuso, F. A., Frankenberg, C., O'Dell, C. W., Brueffe, C. J., Doran, G. B., Eldering, A., Fisher, B. M., Fu, D., Gunson, M. R., Mandrake, L., Osterman, G. B., Schwandner, F. M., Sun, K., Taylor, T. E., , Wennberg, P. O., and Wunch, D.: The on-orbit performance of the Orbiting Carbon Observatory-2 (OCO-2) instrument and its radiometrically calibrated products, Atmospheric Measurement Techniques, 10, 59–81, https://doi.org/10.5194/amt-10-59-2017, 2017.

535 Deng, Z., Ciais, P., Tzompa-Sosa, Z. A., Saunois, M., Qiu, C., Tan, C., Sun, T., Ke, P., Cui, Y., Tanaka, K., Lin, X., Thompson, R. L., Tian, H., Yao, Y., Huang, Y., Lauerwald, R., Jain, A. K., Xu, X., Bastos, A., Sitch, S., Palmer, P. I., Lauvaux, T., d'Aspremont, A., Giron, C., Benoit, A., Poulter, B., Chang, J., Petrescu, A. M. R., Davis, S. J., Liu, Z., Grassi, G., Albergel, C., Tubiello, F. N., Perugini, L., Peters, W., Chevallier, F.: Comparing national greenhouse gas budgets reported in UNFCCC

16

inventories against atmospheric inversions, Earth Syst. Sci. Data, 14, 1639–1675, https://doi.org/10.5194/essd-14-1639-2022, 2022.

Feng, S., F. Jiang, H. Wang, Y. Liu, W. He, H. Wang, Y. Shen, L. Zhang, M. Jia, W. Ju, and J. M. Chen, China's Fossil Fuel CO2 Emissions Estimated Using Surface Observations of Coemitted NO2, *Environmental Science & Technology*, 58 (19), 8299-8312, https://doi.org/10.1021/acs.est.3c07756, 2024.

Gerbig, C.: Parameters for the Vegetation Photosynthesis and Respiration Model VPRM, https://doi.org/10.18160/R9X0-BW7T, 2021.

Goldberg, D.L., Lu, Z., Oda, T., Lamsal, L.N, Liu, F., Griffin, D., McLinden, C.A., Krotkov, N.A., Duncan B.N., Streets, D.G.: Exploiting OMI NO2 satellite observations to infer fossil-fuel CO2 emissions from U.S. megacities, Science of the Total Environment, 695, 122805, https://doi.org/10.1016/j.scitotenv.2019.133805, 2019.

Hase, F., Herkommer, B., Groß, J., Blumenstock, T., Kiel, M. ä ., and Dohe, S., TCCON data from Karlsruhe (DE), Release GGG2020.R1 (Version R1) [Data set]. CaltechDATA. https://doi.org/10.14291/tccon.ggg2020.karlsruhe01.R1, 2023.

ICOS RI, Bergamaschi, P., Colomb, A., De Mazière, M., Emmenegger, L., Kubistin, D., Lehner, I., Lehtinen, K., Leuenberger, M., Lund Myhre, C., Marek, M., Platt, S.M., Plaß-Dülmer, C., Ramonet, M., Schmidt, M., Apadula, F., Arnold, S., Chen, H., Conil, S., Couret, C., Cristofanelli, P., Forster, G., Hatakka, J., Heliasz, M., Hermansen, O., Hoheisel, A., Kneuer, T., Laurila, T., Leskinen, A., Levula, J., Lindauer, M., Lopez, M., Mammarella, I., Manca, G., Meinhardt, F., Müller-Williams, J., Ottosson-Löfvenius, M., Piacentino, S., Pitt, J., Scheeren, B., Schumacher, M., Sha, M.K., Smith, P., Steinbacher, M., Sørensen, L.L., Vítková, G., Yver-Kwok, C., di Sarra, A., Conen, F., Kazan, V., Roulet, Y.-A., Biermann, T., Delmotte, M., Heltai, D., Komínková, K., Laurent, O., Lunder, C., Marklund, P., Pichon, J.-M., Trisolino, P., ICOS Atmosphere Thematic Centre, ICOS ERIC - Carbon Portal, ICOS Flask And Calibration Laboratory (FCL), ICOS Central Radiocarbon Laboratory (CRL), 2022. ICOS Atmosphere Release 2022-1 of Level 2 Greenhouse Gas Mole Fractions of CO_2, CH_4, N_2O, CO, meteorology and $14CO2$. https://doi.org/10.18160/KCYX-HA35

Inness, A., Ades, M., Agustí-Panareda, A., Barré, J., Benedictow, A., Blechschmidt, A., Dominguez, J., Engelen, R., Eskes, H., Flemming, J., Huijnen, V., Jones, L., Kipling, Z., Massart, S., Parrington, M., Peuch, V.-H., Razinger M., Remy, S., Schulz, M. and Suttie, M.: CAMS global reanalysis (EAC4), Copernicus Atmosphere Monitoring Service (CAMS) Atmosphere Data Store (ADS), Accessed on September 1, 2022, https://ads.atmosphere.copernicus.eu/cdsapp#!/dataset/cams-global-reanalysis-eac4?tab=overview, 2019.

IPCC, 2022: Summary for Policymakers [H.-O. Pörtner, D.C. Roberts, E.S. Poloczanska, K. Mintenbeck, M. Tignor, A. Alegría, M. Craig, S. Langsdorf, S. Löschke, V. Möller, A. Okem (eds.)]. In: Climate Change 2022: Impacts, Adaptation and Vulnerability. Contribution of Working Group II to the Sixth Assessment Report of the Intergovernmental Panel on Climate Change [H.-O. Pörtner, D.C. Roberts, M. Tignor, E.S. Poloczanska, K. Mintenbeck, A. Alegría, M. Craig, S. Langsdorf, S. Löschke, V. Möller, A. Okem, B. Rama (eds.)]. Cambridge University Press, Cambridge, UK and New York, NY, USA, pp. 3-33, doi:10.1017/9781009325844.001.

Kaiser, J.W., Heil, A., Andreae, M.O., Benedetti, A., Chubarova, N., Jones, L., Morcrette, J.J., Razinger, M., Schultz, M.G., Suttie, M., and van der Werf, G.R.: Biomass burning emissions estimated with a global fire assimilation system based on observed fire radiative power, Biogeosciences, 9, 527-554, https://doi.org/10.5194/bg-9-527-2012, 2012.

575 Konovalov, I. B., Berezin, E. V., Ciais, P., Broquet, G., Zhuravlev, R. V., and Janssens-Maenhout, G.: Estimation of fossil-fuel CO2 emissions using satellite measurements of "proxy" species, Atmos. Chem. Phys., 16, 13509–13540, https://doi.org/10.5194/acp-16-13509-2016, 2016.

Kuenen, J., Dellaert, S., Visschedijk, A., Jalkanen, J.-P., Super, I., and Denier van der Gon, H.: CAMS-REG-v4: a state-of-the-art high resolution European emission inventory for air quality modelling, Earth System Science Data, 14, 491–515,
580 https://doi.org/10.5194/essd14-491-2022, 2022.

Feng, L., et al.: Consistent regional fluxes of CH4 and CO2 inferred from GOSAT proxy XCH4 : XCO2 retrievals, 2010–2014, Atmos. Chem. Phys., 17, 4781–4797, https://www.atmos-chem-phys.net/17/4781/2017/, 2017.

Fisher, J. A., Murray, L. T., Jones, D. B. A., and Deutscher, N. M.: Improved method for linear carbon monoxide simulation and source attribution in atmospheric chemistry models illustrated using GEOS-Chem v9, Geoscientific Model Development,
585 10, 4129–4144, https://doi.org/10.5194/gmd-10-4129-2017, 2017.

Janssens-Maenhout, G. et al. Toward an operational anthropogenic CO2 emissions monitoring and verification support capacity. Bull. Am. Meteorol. Soc. 101, E1439–E1451, https://doi.org/10.1175/BAMS-D-19-0017.1, 2020.

Landgraf, J., Scheepmaker, R., Borsdorff, T., Hu, H., Houweling, S., Butz, A., Aben, I., Hasekamp, O., et al.: Carbon monoxide total column retrievals from TROPOMI shortwave infrared measurements, Atmospheric Measurement Techniques, 9, 4955–
590 4975, https://doi.org/10.5194/amt-9-4955-2016, 2016.

Lefèvre, N., Tyaquiçã, P., Veleda, D., Perruche, C., & Van Gennip, S. J.: Amazon River propagation evidenced by a CO2 decrease at 8 N, 38 W in September 2013. Journal of Marine Systems, 211, 103419, https://doi.org/10.1016/j.jmarsys.2020.103419, 2020.

Monteil, G., et al.: The regional European atmospheric transport inversion comparison, EUROCOM: first results on European-
595 wide terrestrial carbon fluxes for the period 2006–2015, ACP, 20, 12063–12091, https://doi.org/10.5194/acp-20-12063-2020, 2020.

Notholt, J., Petri, C., Warneke, T., and Buschmann, M., TCCON data from Bremen (DE), Release GGG2020.R0 (Version R0) [Data set]. CaltechDATA. https://doi.org/10.14291/tccon.ggg2020.bremen01.R0, 2022.

600 Oda, T., L. Feng, P. I. Palmer, D. F. Baker, and L. E. Ott, Assumptions about prior fossil fuel inventories impact our ability to estimate posterior net CO2 fluxes that are needed to verifying national inventories, Environ. Res. Lett., 18, 124030, DOI 10.1088/1748-9326/ad059b, 2023.

O'Doherty, S.; Say, D.; Stanley, K.; Young, D.; Stavert, A.; Grant, A.; Ganesan, A.; Pitt, J.; Wenger, A.; Wisher, A.; Garrard, N. (2019): Deriving Emissions related to Climate Change Network: CO2, CH4, N2O, SF6, CO and halocarbon measurements
605 from Tacolneston Tall Tower, Norfolk. Centre for Environmental Data Analysis. https://catalogue.ceda.ac.uk/uuid/ae483e02e5c345c59c2b72ac46574103

O'Doherty, S.; Say, D.; Stanley, K.; Young, D.; Pitt, J.; Wenger, A. (2019): Deriving Emissions related to Climate Change Network: CO_2, CH_4, N_2O, SF_6, CO measurements from Bilsdale Tall Tower, North York Moors National Park. Centre for Environmental Data Analysis. https://catalogue.ceda.ac.uk/uuid/d2090552c8fe4c16a2fd7d616adc2d9f

610 OCO-2 Science Team, Gunson, M., Eldering, A.: OCO-2 Level 2 geolocated XCO2 retrievals results, physical model, Retrospective Processing V10r, Greenbelt, MD, USA, Goddard Earth Sciences Data and Information Services Center (GES DISC), Accessed: December 2022, https://doi.org/10.5067/6SBROTA57TFH, 2020.

Palmer, P. I., Suntharalingam, P., Jones, D. B. A., Jacob, D. J., Streets, D. G., Fu, Q., Vay, S. A., and Sachse, G. W.: Using CO_2:CO correlations to improve inverse analyses of carbon fluxes, J. Geophys. Res., 111, D12318, 615 https://doi.org/10.1029/2005JD006697, 2006.

Palmer, P.I., Feng, L., Baker, D. et al.: Net carbon emissions from African biosphere dominate pan-tropical atmospheric CO2 signal. Nat. Commun., 10, 3344, https://doi.org/10.1038/s41467-019-11097-w, 2019.

Petri, C., Vrekoussis, M., Rousogenous, C., Warneke, T., Sciare, J., Notholt, J., TCCON data from Nicosia (CY), Release GGG2020.R0 (Version R0) [Data set]. CaltechDATA. https://doi.org/10.14291/tccon.ggg2020.nicosia01.R0, 2022.

620 Peylin, P., Law, R.M., Gurney, K.R., Chevallier, F., Jacobson, A.R., Maki, T., Niwa, Y., Patra, P.K., Peters, W., Rayner, P.J., Rödenbeck, C., van der Laan-Luijkx, I. T., and Zhang, X.: Global atmospheric carbon budget: results from an ensemble of atmospheric CO2 inversions, Biogeosciences, 10, 6699–6720, https://doi.org/10.5194/bg-10-6699-2013, 2013.

Ramonet, M., Ciais, P., Apadula, F., Bartyzel, J., Bastos, A., Bergamaschi, P., Blanc, P. E., Brunner, et al.: The fingerprint of the summer 2018 drought in Europe on ground-based atmospheric CO 2 measurements, Philosophical Transactions of the 625 Royal Society B: Biological Sciences, 375, 20190 513, https://doi.org/10.1098/rstb.2019.0513, 2020.

Reuter, M., Buchwitz, M., Schneising, O., Krautwurst, S., O'Dell, C.W., Richter, A., Bovensmann, H., and Burrows, J.P.: Towards monitoring localized CO_2 emissions from space: co-located regional CO_2 and NO_2 enhancements observed by the OCO-2 and S5P satellites, ACP, 19, 9371-9383, https://doi.org/10.5194/acp-19-9371-2019, 2019.

Rödenbeck, C., Zaehle, S., Keeling, R., and Heimann, M.: The European carbon cycle response to heat and drought as seen 630 from atmospheric CO2 data for 1999–2018, Phil. Trans. R. Soc. B, 375: 20190506, http://doi.org/10.1098/rstb.2019.0506, 2020.

Scholze, M., Kaminski, T., Knorr, W.,Voßbeck, M., Wu, M., Ferrazzoli, P., et al.: Mean European carbon sink over 2010–2015 estimated by simultaneous assimilation of atmospheric CO2, soil moisture, and vegetation optical depth. Geophys. Res. Lett., 46, 13, 796–13, 803, https://doi.org/10.1029/2019GL085725, 2019.

635 Silva, S., Arellano, A.F., and Worden, H.M.: Toward anthropogenic combustion emission constraints from space-based analysis of urban CO2/CO sensitivity, Geophysical Research Letters, 40, 4971-4976, https://doi.org/10.1002/grl.50954, 2013.

Sierk, B., Fernandez, V., Bézy, J.-L., Meijer, Y., Durand, Y., Bazalgette Courrèges-Lacoste, G., Pachot, C., Löscher, A., Nett, H., Minoglou, K., Boucher, L., Windpassinger, R., Pasquet, A., Serre, D., and te Hennepe, F.: The Copernicus CO2M Mission for Monitoring Anthropogenic Carbon Dioxide Emissions from Space, in: International Conference on Space Optics – ICSO 640 2020, 30 March–2 April 2021, virtual meeting, SPIE, vol. 11852, 1563–1580, https://doi.org/10.1117/12.2599613, 2021.

Stanley, K. M., Grant, A., O'Doherty, S., Young, D., Manning, A. J., Stavert, A. R., Gerard Spain, T., Salameh, P. K., Harth, C. M., Simmonds, P. G., Sturges, W. T., Oram, D. E., and Derwent, R. G.: Greenhouse gas measurements from a UK network of tall towers: Technical description and first results, Atmospheric Measurement Techniques, 11, 1437–1458, https://doi.org/10.5194/amt-11-1437-2018, 2018.

645 Suntharalingam, P., J. T. Randerson, N. Krakauer, J. A. Logan, and D. J. Jacob, Influence of reduced carbon emissions and oxidation on the distribution of atmospheric CO2: Implications for inversion analyses, Global Biogeochem. Cycles, 19, GB4003, doi:10.1029/2005GB002466, 2005.

Super, I., Dellaert, S. N. C., Visschedijk, A. J. H., and Denier van der Gon, H.: Uncertainty analysis of a European high-resolution emission inventory of CO_2 and CO to support inverse modelling and network design, Atmospheric Chemistry and

650 Physics, 20, 1795–1816, https://doi.org/10.5194/acp-20-1795-2020, 2020.

Super, I., Scarpelli, T., Droste, A., and Palmer, P. I.: Improved definition of prior uncertainties in CO_2 and CO fossil fuel fluxes and the impact on a multi-species inversion with GEOS-Chem (v12.5), EGUsphere [preprint], https://doi.org/10.5194/egusphere-2023-2025, 2024.

Taylor, T. E., O'Dell, C. W., Baker, D., Bruegge, C., Chang, A., Chapsky, L., Chatterjee, A., Cheng, C., Chevallier, F., Crisp,

655 D., Dang, L., Drouin, B., Eldering, A., Feng, L., Fisher, B., Fu, D., Gunson, M., Haemmerle, V., Keller, G. R., Kiel, M., Kuai, L., Kurosu, T., Lambert, A., Laughner, J., Lee, R., Liu, J., Mandrake, L., Marchetti, Y., McGarragh, G., Merrelli, A., Nelson, R. R., Osterman, G., Oyafuso, F., Palmer, P. I., Payne, V. H., Rosenberg, R., Somkuti, P., Spiers, G., To, C., Weir, B., Wennberg, P. O., Yu, S., and Zong, J.: Evaluating the consistency between OCO-2 and OCO-3 XCO2 estimates derived from the NASA ACOS version 10 retrieval algorithm, Atmos. Meas. Tech., 16, 3173–3209, https://doi.org/10.5194/amt-16-3173-

660 2023, 2023.

Té, Y., Jeseck, P., and Janssen, C., TCCON data from Paris (FR), Release GGG2020.R0 (Version R0) [Data set]. CaltechDATA. https://doi.org/10.14291/tccon.ggg2020.paris01.R0, 2022.

Thompson, R. L., Broquet, G., Gerbig, C., Koch, T., Lang, M., Monteil, G., Munassar, S., Nickless, A., Scholze, M., Ramonet, M., Karstens, U., van Schaik, E., Wu, Z. and Rödenbeck, C.: Changes in net ecosystem exchange over Europe during the 2018

665 drought based on atmospheric observations, Phil. Trans. R. Soc. B, 375: 20190512, https://doi.org/10.1098/rstb.2019.0512, 2020.

Veefkind, J., Aben, I., McMullan, K., Förster, H., De Vries, J., Otter, G., Claas, J., Eskes, H., De Haan, J., Kleipool, Q., et al.: TROPOMI on the ESA Sentinel-5 Precursor: A GMES mission for global observations of the atmospheric composition for climate, air quality and ozone layer applications, Remote Sensing of the Environment, 120, 70–83,

670 https://doi.org/10.1016/j.rse.2011.09.027, 2012.

Vidot, J., Landgraf, J., Hasekamp, O., Butz, A., Galli, A., Tol, P., and Aben, I.: Carbon monoxide from shortwave infrared reflectance measurements: A new retrieval approach for clear sky and partially cloudy atmospheres, Remote sensing of environment, 120, 255–266, https://doi.org/10.1016/j.rse.2011.09.032, 2012.

Warneke, T., Petri, C., Notholt, J., and Buschmann, M., TCCON data from Orléans (FR), Release GGG2020.R0 (Version R0)
675   [Data set]. CaltechDATA. https://doi.org/10.14291/tccon.ggg2020.orleans01.R0, 2022.

White, E.D., Rigby, M., Lunt, M.F., Smallman, T.L., Comyn-Platt, E., Manning, A.J., Ganesan, A.L., Simon O'Doherty, S., Stavert, A.R., Stanley, K., Williams, M., Levy, P., Ramonet, M., , Forster, G.L., Manning, A.C., and Palmer, P.I.: Quantifying the UK's carbon dioxide flux: an atmospheric inverse modelling approach using a regional measurement network, Atmos. Chem. Phys., 19, 4345-4365, https://doi.org/10.5194/acp-19-4345-2019, 2019.

680   Yang, E.G., Kort, E.,A. Ott, L.E., Oda, T., Lin, J.C.: Using Space-Based CO2 and NO2 Observations to Estimate Urban CO2 Emissions, JGR Atmospherers,128, 6, https://doi.org/10.1029/2022JD037736, 2023.

Table 1. Average domain CO_2 combustion emissions for 2018-2021

685

	Mean (Gt a^{-1})		RSD [a] (%)
	Emission	Change [a]	
A priori[b]	4.9		2.4
TNO *a priori*[b]	4.9		1.6
Satellite			690
CO_2-only	4.9	-	2.4
Joint CO_2:CO[c]	4.6	▼	2.1
TNO CO_2:CO[c]	4.8	-	1.6
In-situ			
CO_2-only	4.8	▼	2.2
Joint CO_2:CO	5.0	▲	2.2
TNO CO_2:CO	4.9	-	1.5

[a]The arrows indicate the change of the mean from the *a priori*. Blue-downward pointing arrows show a decrease, red-upward show an increase, and grey dashes show no change. RSD stands for relative standard deviation.

[b]The *a priori* uncertainty labelled as '*A priori*' is for the CO_2-only and joint inversions, so we also include the *a priori* uncertainty for the TNO inversion.

[c]The Joint and TNO satellite inversions only include July 2018 - December 2021. The *a priori* combustion emission for this period is 4.8 Gt a^{-1} so we show no change for the TNO *a posteriori* emissions.
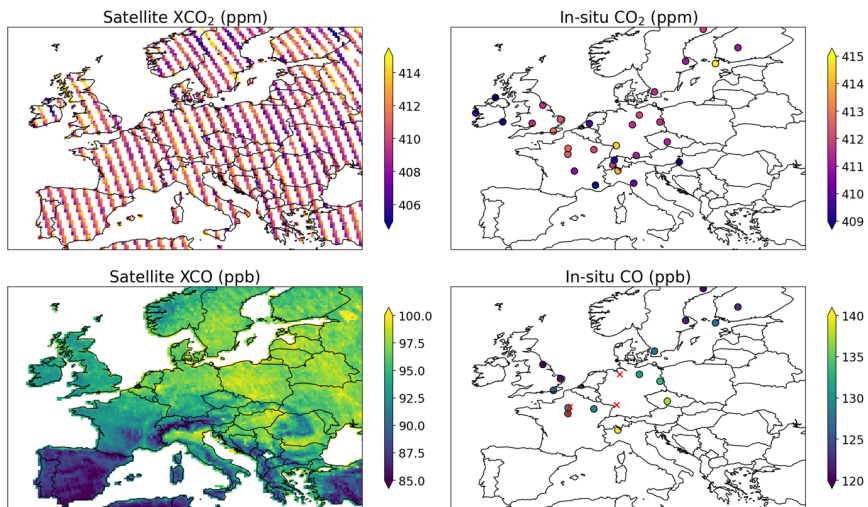
Figure 1. Annual mean CO₂ and CO observed by satellite and *in situ* networks across Europe for 2018-2021. Satellite observations of XCO₂ and XCO are from OCO-2 and TROPOMI, respectively, and *in situ* observations are from the DECC and ICOS networks. The red X points in the *in situ* CO plot show the locations of the four out of the five TCCON sites for which we use XCO₂ and XCO data to evaluate our inversions; the fifth site, based in Cyprus is located outside the figure domain. The observations are filtered as stated in the text and satellite observations are shown at 0.25° x 0.3125° resolution. TROPOMI observations only include observations after July 2018.

CO₂ff flux (10⁻⁸ kg m⁻²s⁻¹)

CO₂bio flux (10⁻⁸ kg m⁻²s⁻¹)

COff flux (10⁻¹⁰ kg m⁻²s⁻¹)
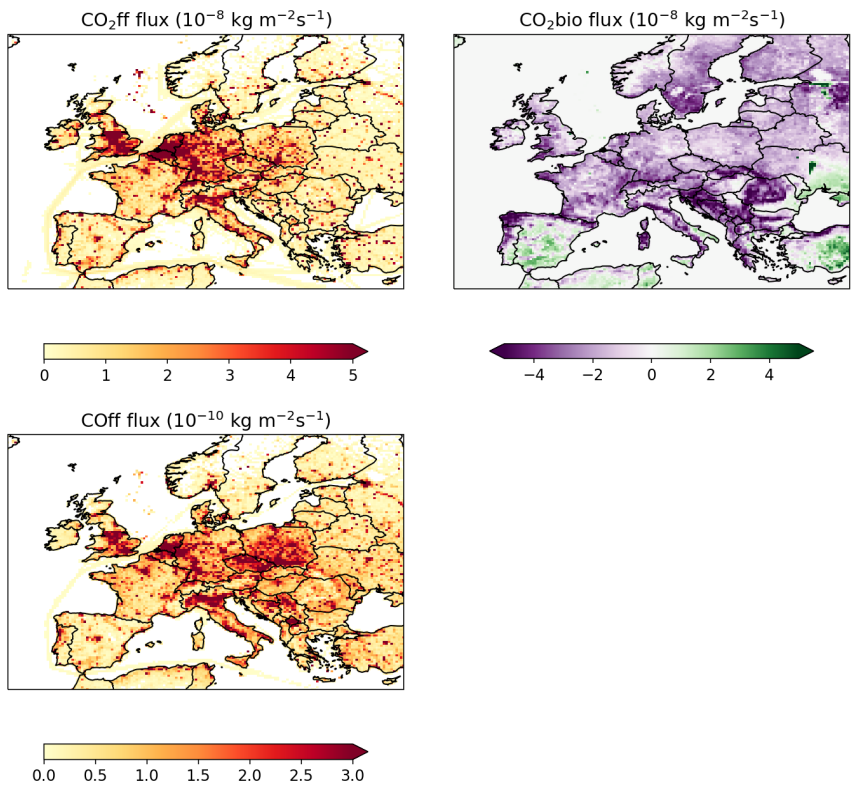
710

Figure 2. Annual mean emissions for 2018-2021 in the *a priori* inventories. Combustion emissions (CO₂^{combust}, CO^{combust}) are from the TNO inventory while biogenic fluxes (CO₂^{bio}) are from the VPRM model (negative values indicate a CO₂ sink).
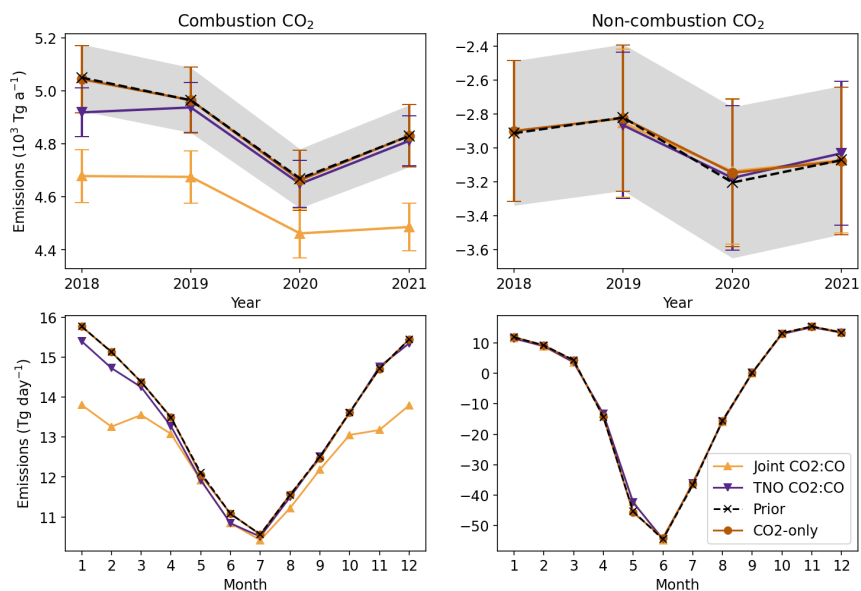
715

24

Figure 3. Annual and monthly mean European CO₂ combustion and non-combustion emissions inferred from satellite inversions for 2018-2021. The non-combustion emissions include biogenic and non-combustion anthropogenic emission sources. The top row shows annual mean CO₂ flux estimates by inversion type, with errors bars showing the 1-σ errors except for the *a priori* errors which are shown as a shaded region. The bottom row shows monthly mean fluxes for 2018-2021. The TNO and joint inversions only include July 2018-December 2021 for combustion and 2019-2021 for non-combustion. Please note differences in the range used for the y axes.
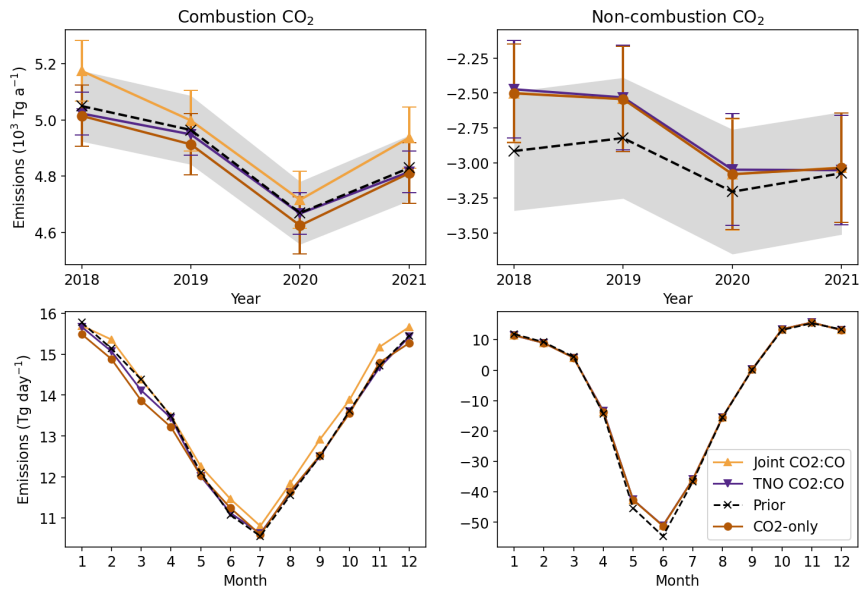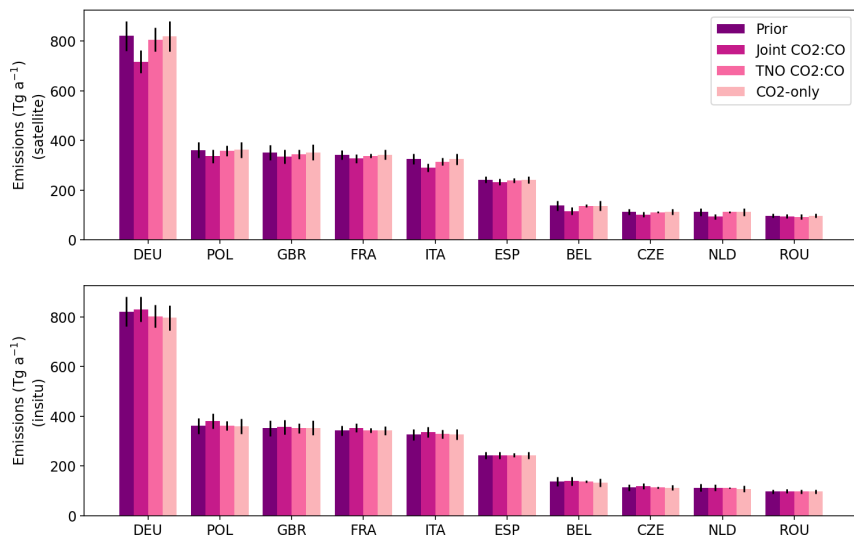
Figure 4. The same as Figure 4 for *in situ* inversions.

725

26

Figure 5. Annual mean *a priori* and *a posteriori* CO₂ combustion emissions by country for satellite (top) and *in situ* (bottom) inversions. We show the top 10 emitting countries in our European domain with emissions averaged over 2018-2021. The TNO and joint satellite inversion averages do not include dates prior to July 2018.
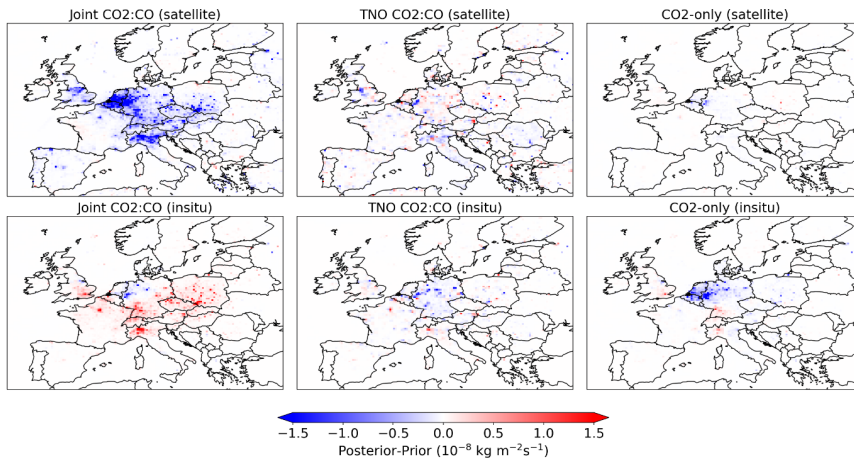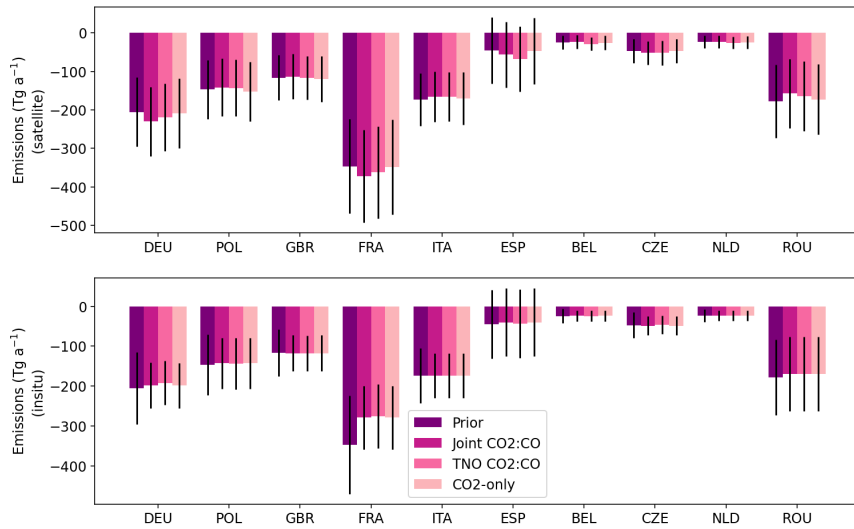
Figure 6. Annual mean CO₂ combustion emissions difference (*a posteriori* minus *a priori*) for satellite (top row) and *in situ* (bottom row) inversions, 2018-2021, shown at the native model resolution of 0.25° x 0.3125°. The TNO and joint satellite inversion averages do not include dates prior to July 2018.

Figure 7. As Figure 5 but for non-combustion CO₂ fluxes estimates. The TNO and joint satellite inversion averages do
745 **not include 2018. The non-combustion emissions include biogenic and non-combustion anthropogenic emission sources.**
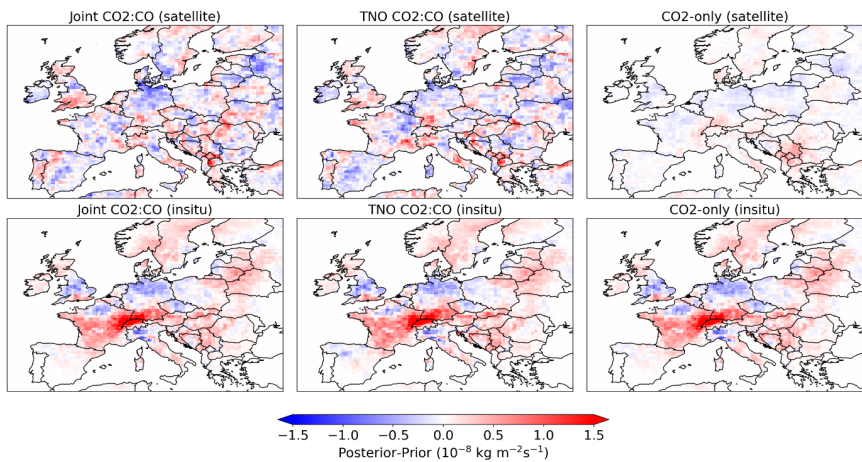
Figure 8. As Figure 6 but for non-combustion CO₂ flux estimates. The TNO and joint satellite inversion averages do not include 2018. The non-combustion emissions include biogenic and non-combustion anthropogenic emission sources.

30

Appendix A

1 Description of an *a priori* ensemble generation

760   For the *a priori* ensemble perturbations that represent our state vector ($\mathbf{x}_n^b$ for the *n*th ensemble member), we generate an ensemble of scale factors based on the desired error statistics, described in Section 2.3. For the combustion and non-combustion scale factors, we solve for scale factors on a 0.5° x 0.625° resolution grid (double our nested model resolution). Each ensemble member is then a grid of perturbations that we will apply to our emissions grid. To generate the ensemble members, we first generate an error covariance matrix (**P**):

765

$$\mathbf{P} = \mathbf{P}' \cdot \left(e^{-\frac{\mathbf{D}}{100}} \cdot \mathbf{P}' \right),$$

where $\mathbf{P}'$ is a diagonal matrix with the variance for each state vector element along its diagonal. Covariance between grid cells is based on the spatial proximity between each grid cell and its neighbor with distances between grid cells represented by the

770   matrix $\mathbf{D}$. The influence of neighboring grid cells decreases with distance following an exponential decay with a length scale of 100 km, assuming isotropy.

We then perform a Cholesky decomposition on **P**. We generate each *a priori* ensemble member by applying a random perturbation vector with mean zero and standard deviation equal to one ($\mathbf{\eta}$) to the decomposed matrix (**L**) and adding one

775   (which is the assumed *a priori* mean of all ensemble members):

$$\mathbf{x}_n^b = 1 + \mathbf{L} \cdot \mathbf{\eta}.$$

The TNO emissions inventory is constructed by allocating national emissions to a grid using a spatial map of activity data

780   (e.g., a population map), so the uncertainty in the gridded emission estimate is a combination of the uncertainty in the national emissions and the uncertainty in the spatial product used to distribute emissions. We use uncertainty estimates for the national emissions, uncertainties for the spatial products, and estimates of the correlation of uncertainties for the two species to generate an ensemble of gridded emissions by sector, following a Monte Carlo approach. This method is described in Super et al. (2023). We use the emissions ensemble to generate an error covariance matrix (**P**) and follow the steps outlined in the main text.

785

Table A1. Fit of *a priori* and *a posteriori* modelled CO_2 compared to observations for 2018-2021[a]

	Correlation coefficient			Relative mean bias (%)		
	In situ	TCCON[b]	Satellite	*In situ*	TCCON	Satellite
A priori	0.76	0.87	0.84	0.2	0.7	0.2
Satellite inversions						
CO$_2$-only	0.81	0.90	0.92	-0.2	0.4	-0.1
Joint CO$_2$:CO[c]	0.80	0.93	0.95	-0.2	0.5	<0.05
TNO CO$_2$:CO[c]	0.82	0.92	0.95	-0.1	0.5	<0.05
In situ inversions						
CO$_2$-only	0.83	0.85	0.85	-0.4	0.2	-0.2
Joint CO$_2$:CO	0.84	0.85	0.86	-0.3	0.4	-0.1
TNO CO$_2$:CO	0.84	0.86	0.87	-0.3	0.3	-0.1

[a]We use the Pearson's correlation coefficient and relative mean bias (the means of the *a posteriori* and *a priori* difference divided by the *a priori*) as measures of fit. [b]Five sites are within our domain (Figure 2) include Bremen (Germany), Karlsruhe (Germany), Nicosia (Cyprus), Orléans (France), and Paris (France).

810 **Table A2. Annual mean national CO$_2$ combustion emissions (Emis; Tg a^{-1}) and relative standard deviations (RSD; %) for 2018-2021 satellite inversions**

Country	Country Abbr.	Prior		CO$_2$-only		Joint[a]		TNO[a,b]		
		Emis	RSD	Emis	RSD	Emis	RSD	Emis	RSD	PRSD
Germany	DEU	821	7	819	7	717	6	806	6	6
Poland	POL	361	9	362	9	336	8	358	5	5
United Kingdom	GBR	351	9	352	9	335	8	345	5	6
France	FRA	342	6	343	6	327	5	338	2	2
Italy	ITA	326	7	325	7	291	6	314	5	5
Spain	ESP	242	6	242	6	233	5	239	4	4
Belgium	BEL	137	14	137	14	116	13	136	4	4
Czech Republic	CZE	113	11	113	11	102	10	111	3	3
Netherlands	NLD	112	13	112	13	93	12	112	2	3
Romania	ROU	97	8	97	8	95	8	93	10	10

[a]The satellite inversions that include CO only show means for July 2018 - December 2021.

[b]The *a priori* uncertainties for TNO differ from the CO$_2$-only and joint inversions, so we list the TNO *a priori* uncertainties (PRSD) as well. The higher *a posteriori* error for Romania is due to the error inflation factor used in the sequential inversion.

815

Table A3. Annual mean national CO$_2$ combustion emissions (Emis; Tg a^{-1}) and relative standard deviations (RSD; %) for 2018-2021 *in situ* inversions[a]

Country	Country Abbr.	CO$_2$-only		Joint		TNO	
		Emis	RSD	Emis	RSD	Emis	RSD
Germany	DEU	796	6	830	6	802	6
Poland	POL	360	8	380	8	361	5
United Kingdom	GBR	353	8	356	8	352	6
France	FRA	342	5	353	5	342	2
Italy	ITA	327	6	336	6	328	5
Spain	ESP	243	6	243	6	243	3
Belgium	BEL	132	13	139	12	137	4
Czech Republic	CZE	112	10	119	10	113	3
Netherlands	NLD	107	12	112	12	112	2
Romania	ROU	97	8	98	8	97	9

[a]Only the *a posteriori* emissions are shown. The *a priori* emissions and uncertainties are listed in Table A2.

820

Table A4. Domain mean CO_2 non-combustion emissions for 2018-2021[a]

	Mean (Gt a^{-1})	RSD (%)	
			825
A priori	-3.0	14	
Satellite			
CO_2-only	-3.0	14	
Joint CO_2:CO[b]	-3.0	14 830	
TNO CO_2:CO[b]	-3.0	14	
In-situ			
CO_2-only	-2.8	14	
			835
Joint CO_2:CO	-2.8	14	
TNO CO_2:CO	-2.8	14	

[a] The non-combustion emissions include biogenic and non-combustion anthropogenic emission sources.

840   [b]Joint and TNO inversion satellite results only include 2019-2021. The *a priori* non-combustion flux is the same for this period (-3.0 Gt a^{-1}).
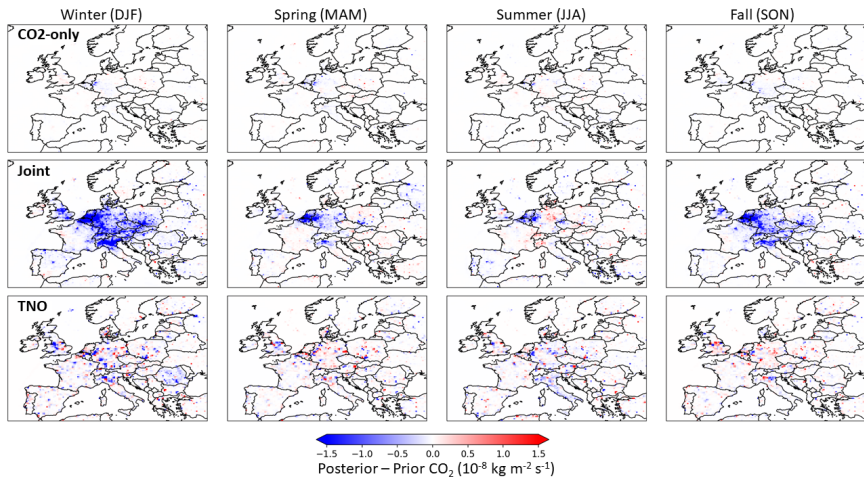
Figure A1. Seasonal mean *a posteriori* and *a priori* CO₂ combustion emissions difference for satellite inversions for 2018-2021. The inversions including CO satellite observations do not include emissions differences prior to July 2018.
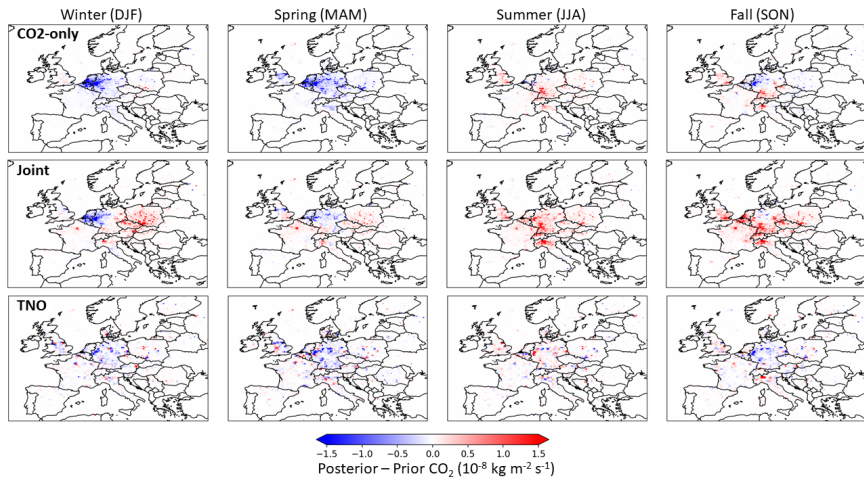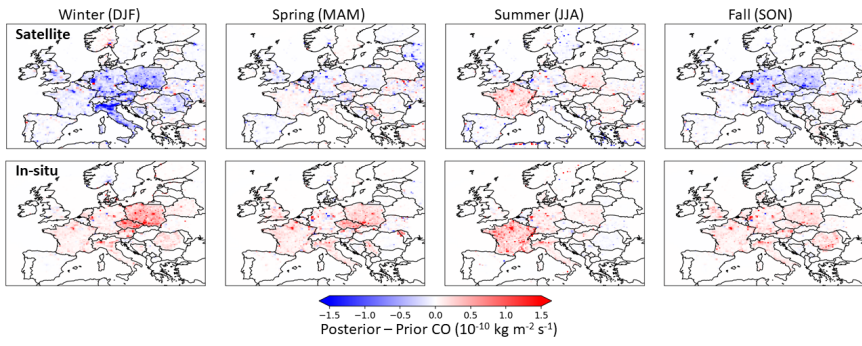
Figure A2. Same as Figure A1 for *in situ* inversions.

Figure A3. Same as Figure A1 for CO in satellite and *in situ* inversions.

855

38